MATERIALS SCIENCE

Structural and spectral dynamics of single-crystalline Ruddlesden-Popper phase halide perovskite blue light-emitting diodes

Hong Chen[1,2,3]*, Jia Lin[1,4]*, Joohoon Kang[1,5,6,7,8]*, Qiao Kong[1], Dylan Lu[1], Jun Kang[9], Minliang Lai[1], Li Na Quan[1,9], Zhenni Lin[9,10], Jianbo Jin[1], Lin-wang Wang[9], Michael F. Toney[2]†, Peidong Yang[1,7,9,10]†

Achieving perovskite-based high–color purity blue-emitting light-emitting diodes (LEDs) is still challenging. Here, we report successful synthesis of a series of blue-emissive two-dimensional Ruddlesden-Popper phase single crystals and their high–color purity blue-emitting LED demonstrations. Although this approach successfully achieves a series of bandgap emissions based on the different layer thicknesses, it still suffers from a conventional temperature-induced device degradation mechanism during high-voltage operations. To understand the underlying mechanism, we further elucidate temperature-induced device degradation by investigating the crystal structural and spectral evolution dynamics via in situ temperature-dependent single-crystal x-ray diffraction, photoluminescence (PL) characterization, and density functional theory calculation. The PL peak becomes asymmetrically broadened with a marked intensity decay, as temperature increases owing to $[PbBr_6]^{4-}$ octahedra tilting and the organic chain disordering, which results in bandgap decrease. This study indicates that careful heat management under LED operation is a key factor to maintain the sharp and intense emission.

INTRODUCTION

Conventional three-dimensional (3D) metal halide perovskites with an ABX_3 formula [A = cations such as Cs^+, methylammonium (MA^+), or formamidinium (FA^+); B = Pb^{2+} or Sn^{2+}; X = Cl^-, Br^-, or I^-] are of great interest for optoelectronics due to their excellent properties, such as high emission efficiencies, long carrier diffusion lengths, high absorption coefficient, and defect tolerance (*1*–*3*). Recently, the 3D perovskite-based light-emitting diode (LED) applications have demonstrated a rapid progress in red and green light emission with external quantum efficiencies (EQEs) of more than 20% (*4*, *5*). However, blue-emitting LEDs still have remaining challenges mainly due to the limited number of color-stable blue-emissive perovskite compositions, which require further chemical or structural engineering.

A conventional method of synthesizing blue-emissive material is bandgap tuning by controlling the mixed halogen component (i.e., Cl-Br mixed halide perovskites). The bandgap of these perovskites is monotonically tunable based on the ratio of mixed halogen ions. However, the halogen ion migration induces Cl-rich and Br-rich phase segregation under LED device operation and causes undesired electroluminescence (EL) wavelength shift from blue to green (*6*). Another approach is producing wide-bandgap 2D perovskites via structural engineering such as 2D Ruddlesden-Popper (RP) phase perovskites with a general formula of $A'_2A_{n-1}B_nX_{3n+1}$ (A′ is long-chain ammonium, A is the small cations in the perovskite, B represents the metal cations, X is the halide ions, and *n* represents the number of octahedra layers in between long-chain ligands A′) (*7*–*9*). This structure consisted of ordered single-crystalline semiconductor domains with tunable thickness separated by organic insulating species such as BA^+ (BA^+ stands for *n*-butylammonium) (*10*–*12*). By increasing *n*, the bandgaps of the RP perovskites with a composition of $(BA)_2MA_{n-1}Pb_nI_{3n+1}$ are tunable from 2.38 eV (*n*1), 2.17 eV (*n*2), 2.03 eV (*n*3), 1.91 eV (*n*4), 1.83 eV (*n*5), and 1.59 eV (*n*∞, 3D), crossing the green and red light emission range, while the LED devices based on these materials are only in thin-film form (*11*, *13*). Moreover, unlike the 3D perovskite-based LED applications, it is still challenging to demonstrate color-stable LEDs due to the formation of mixed phases, as the main technical limitation during the device fabrication is that a conventional spin-coating process induces A-site cation segregation and consequence mixed layer numbers from *n*2 to *n*∞ in the obtained film. So far, with the mixed phases present in the previous demonstrated green- and red-emitting RP phase–based devices, the energy funneling from larger bandgaps to the smallest bandgap allows the achievement of efficient light emitting in long wavelengths (*8*, *14*–*17*), achieving impressive EQEs exceeding 14% (green) and 11% (red). However, the energy funneling–induced color drift makes it difficult to achieve stable violet or blue wide-bandgap RP perovskite–based LEDs (*18*, *19*); the only stable sky blue emission case, based on our knowledge, has been demonstrated by exploiting two cations to control the crystallization and domain layer thickness distributions (*18*, *19*).

Here, we have successfully synthesized and solved the crystal structures of a series of pure-phase Br-based single-crystal RP phases $A'_2A_{n-1}B_nX_{3n+1}$, where A cation is Cs, i.e., $(BA)_2Cs_{n-1}Pb_nBr_{3n+1}$ (n = 1, 2, 3, denoted as *n*1, *n*2, *n*3, respectively). On the basis of the layer number, a sharp emission spectrum has been shown at different wavelengths in the blue range from 416, 445, to 473 nm, which

[1]Department of Chemistry, University of California, Berkeley, Berkeley, CA, USA. [2]Stanford Synchrotron Radiation Light Source, SLAC National Accelerator Laboratory, Stanford University, Menlo Park, CA, USA. [3]School of Environmental Science and Engineering, Southern University of Science and Technology, Shenzhen, Guangdong, China. [4]Department of Physics, Shanghai University of Electric Power, Shanghai, China. [5]Center for Nanomedicine, Institute for Basic Science (IBS), Seoul, South Korea. [6]Y-IBS Institute, Yonsei University, Seoul, South Korea. [7]Kavli Energy NanoScience Institute, Berkeley, CA, USA. [8]School of Advanced Materials Science and Engineering, Sungkyunkwan University (SKKU), Suwon, South Korea. [9]Materials Sciences Division, Lawrence Berkeley National Laboratory, Berkeley, CA, USA. [10]Department of Materials Science and Engineering, University of California, Berkeley, Berkeley, CA, USA.
*These authors contributed equally to this work.
†Corresponding author. Email: mftoney@slac.stanford.edu (M.F.T.); p_yang@berkeley.edu (P.Y.)

corresponds to *n*1, *n*2, and *n*3 bandgaps, respectively. Furthermore, we demonstrate blue-emitting LED devices based on the RP single crystals that we achieved via a micromechanical exfoliation approach. Unlike the previous spin coating–based approaches, our LED device exhibits high color pure blue EL emissions, which were well matched with the intrinsic bandgaps. However, these wide-bandgap RP perovskites are not electrically conductive and thus induce a significant amount of heating at the junctions resulting in structural degradation of the RP crystals. To gain fundamental insights into the heat-induced crystal degradation under LED operation, we collected temperature-dependent in situ photoluminescence (PL) spectra, which show peak intensity weakening and broadening as temperature increases. Furthermore, temperature-dependent in situ single-crystal x-ray diffraction (SCXRD) and density functional theory (DFT) calculation were used to further support the structural and spectral dynamics in the atomic scale of these RP phase single crystals.

RESULTS AND DISCUSSION

Pure-phase single-crystalline $(BA)_2Cs_{n-1}Pb_nBr_{3n+1}$ (*n*1 to *n*3) RP phase matrix single crystals were synthesized in a gram scale via a solution-based synthesis method from BABr, CsBr, and $PbBr_2$ raw materials in a concentrated HBr acid solution by carefully tuned BA/Cs/Pb ratios, as detailed in the Supplementary Materials. For higher layer numbers (i.e., $n \geq 4$), we found mixed $n = 1 - \infty$ phases (fig. S1) and an additional impurity phase of $CsPb_2Br_5$ (125 phase). A possible reason for the mixed phase for the large layer numbers is that the thermodynamic stability energy difference between different layer numbers in the Cs-based RP crystal is smaller than the previously demonstrated MA-based version in the $(BA)_2MA_{n-1}Pb_nI_{3n+1}$ crystals, as the layer number increases (*11*, *13*, *20*, *21*). The crystal structures of the synthesized $(BA)_2Cs_{n-1}Pb_nBr_{3n+1}$ (*n*1 to *n*3) were evaluated by a synchrotron-based SCXRD at 100 K, and all the selected crystallographic information are listed in table S1. As shown in Fig. 1, the inorganic layer of *n*1 is composed of one layer of $[PbBr_6]^{4-}$ octahedra, and *n*2 and *n*3 are constructed by two and three layers of the octahedra, respectively. On the A-site of *n*2 and *n*3 octahedra layers, Cs^+ cations are incorporated inside, providing a driving force to stabilize the octahedra layers by partially balancing the negative charges among the $[PbBr_6]^{4-}$ octahedra. The compositions of the as-synthesized $(BA)_2Cs_{n-1}Pb_nBr_{3n+1}$ single crystals were confirmed with energy-dispersive x-ray (EDX) spectroscopy, with average Cs/Pb/Br ratios of 0:1:3.86 for *n*1, 1:2.26:7.61 for *n*2, and 2:2.77:10.39 for *n*3, respectively (fig. S2). Considering the intrinsic error in EDX, these results are within the expected atomic ratios for the different *n*-value RP phases and are consistent with the refinement results obtained from SCXRD.

As compared with the direct deposition of different composition RP phase thin films or colloidal nanocrystals resulting in mixed phases and complex compositions, our high-quality single crystals provide a good platform for the study of optical and electrical properties of different RP phases. Figure 2A shows the ultraviolet-visible (UV-vis) spectra of *n*1, *n*2, and *n*3 phases. With increasing *n*, the optical bandgap decreases from 2.97 eV (*n*1), 2.77 eV (*n*2), to 2.59 eV (*n*3). This bandgap-decreasing tendency with larger *n* is consistent with the behavior in the $(BA)_2(MA)_{n-1}Pb_nI_{3n+1}$ family.

PL spectra of these single crystals have been measured at room temperature (Fig. 2b). By increasing *n*, the emission color (peak) moved from violet (*n*1, 416 nm), blue (*n*2, 445 nm), to light blue (*n*3, 473 nm) across the blue wavelength range and consistent with

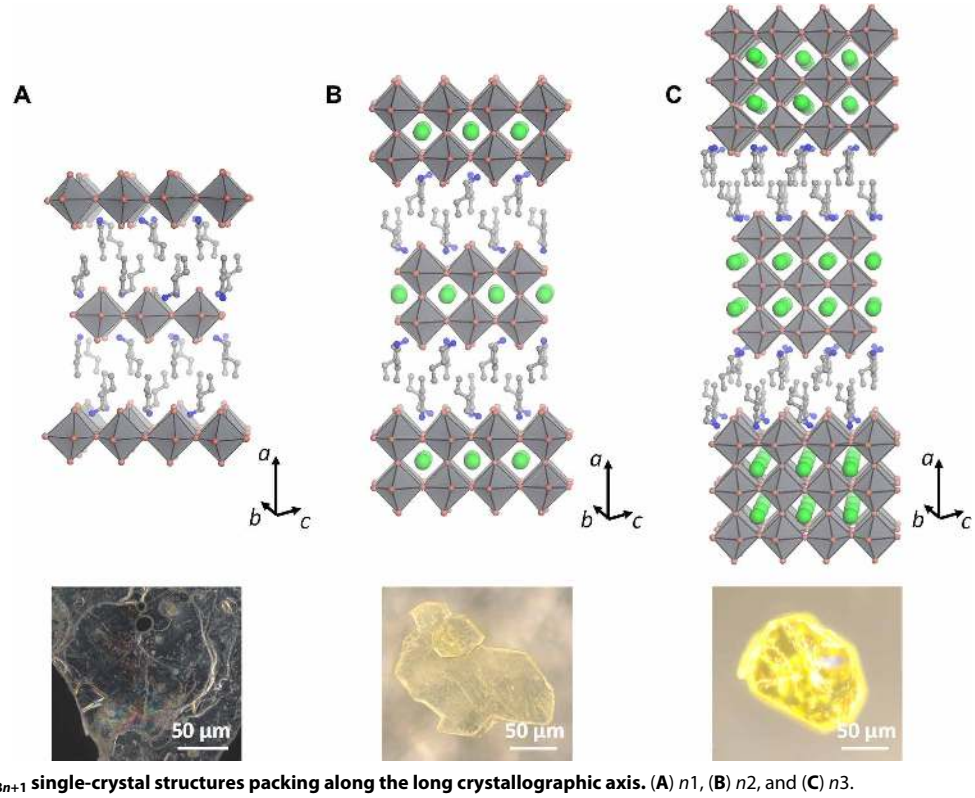

Fig. 1. $(BA)_2Cs_{n-1}Pb_nBr_{3n+1}$ single-crystal structures packing along the long crystallographic axis. (**A**) *n*1, (**B**) *n*2, and (**C**) *n*3.

the optical bandgaps obtained based on the excitonic contribution from UV-vis spectra. This emission behavior confirms our hypothesis that structural engineering of the thickness of the metal-halide octahedral perovskite layers generates RP phases of suitable *n* with the band edge located at the center of blue emission energy. The corresponding CIE (International Commission on Illumination) coordinate is plotted in Fig. 2C. The CIE coordinate of the *n*2 crystal is located most closely to the standard blue emission. The peak intensity of *n*1 to *n*3 phases decreases with increasing *n* but is significantly stronger than the *n*∞ emission. The PL quantum yield is measured to be 15.6, 1.7, and 1.2% for *n*1, *n*2, and *n*3 phases, respectively, with a clear decreasing trend as *n* increases, indicating the confined structure-induced exciton binding energy differences. As the temperature decreases from room temperature down to 4 K, the *n*1 phase shows a PL peak shift of 3.8 nm, while *n*2 and *n*3 phases show negligible peak shift due to the relatively weaker exciton binding energy with increasing *n* (fig. S4). A photocurrent measurement for each layer number provides other evidence that the photogenerated excitons can be more effectively dissociated with the weaker exciton binding energy of the *n*3 phase (fig. S5). The long tail of PL emission of the *n*1 phase at high wavelength is a characteristic feature of the RP phase perovskites, which can be ascribed to trap emission (*22*). The tail intensity in *n*2 and *n*3 phases decreased significantly, suggesting superior optoelectronic properties for larger *n*-value RP phases. This can be further confirmed by the time-resolved PL decay measurement. As shown in Fig. 2D, the decay curves of these single crystals show a biexponential feature. By fitting the decay curves, the longer-time carrier recombination lifetime is determined to be 2.9 ± 0.3, 6.8 ± 0.5, and 15.4 ± 1.0 ns for *n*1, *n*2, and *n*3 phases, respectively, which increases with increasing *n*. We also tracked the PL spectra of the *n*3 phase after the single crystals were exposed to air with about 50% relative humidity (fig. S6). It reveals that the PL emission peak of the pure-phase single crystal is stable up to 6 months without any additional peaks. Only PL emission intensity gradually decreases, probably due to the surface passivation after exposure to air for a long time. The high moisture stability is contributed by the hydrophobic effect of the organic head groups and benefits from the Cs^+ cations in the perovskite layers, which combine with the $[PbBr_6]^{4-}$ octahedra to make the perovskite layers purely inorganic (*23*).

To evaluate EL characteristics of as-synthesized RP single crystals, we used a conventional layered LED device structure. However, an emitting layer was prepared via a micromechanical exfoliation method to keep their single crystallinity. Followed by the crystal exfoliation on poly(3,4-ethylenedioxythiophene):poly(styrenesulfonate) (PEDOT:PSS)–coated prepatterned indium tin oxide (ITO) substrates, an organic electron transport layer [35-nm TPBi (2,2′,2″-(1,3,5,-benzinetriyl)-tris(1-phenyl-1*H*-benzimidazole)] and cathode (1-nm LiF/100-nm Al) are sequentially deposited via thermal evaporation under ultrahigh vacuum. A cross-sectional scanning electron microscopy (SEM) image of the device structure (ITO/PEDOT:PSS/RP/TPBi/LiF/Al) is shown in Fig. 3A. Here, the exfoliated perovskite nanosheets are embedded in the organic TPBi layer having a wide bandgap of ~3.4 eV as a charge hosting layer. A schematic energy band diagram is also shown in Fig. 3A. Figure 3B is an atomic force microscopy (AFM) image of the micromechanically exfoliated nanosheets with an average thickness of 34 nm. While our approach can avoid the mixed *n*-layer phase formation, the nonuniformity and surface coverage should be addressed in the future. The EL spectra of *n*2 (blue line) and *n*3 (sky blue line) single crystal–based LED are observed at 450 and 482 nm with a full width at half-maximum of 27.5 and 18.1 nm, respectively (Fig. 3C). We

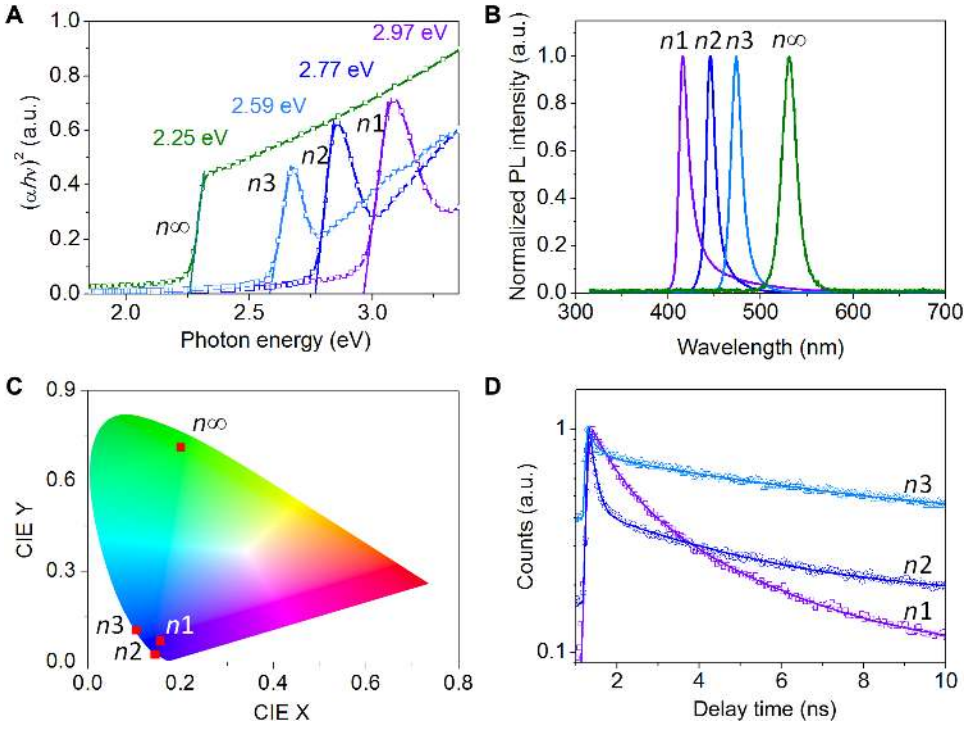

Fig. 2. Optical characterizations of $(BA)_2Cs_{n-1}Pb_nBr_{3n+1}$ (*n*1 to *n*3) single crystals. (**A**) UV-vis spectra; (**B**) normalized PL emission spectra; (**C**) CIE coordinate; (**D**) time-resolved PL decay spectra and fitting curves.

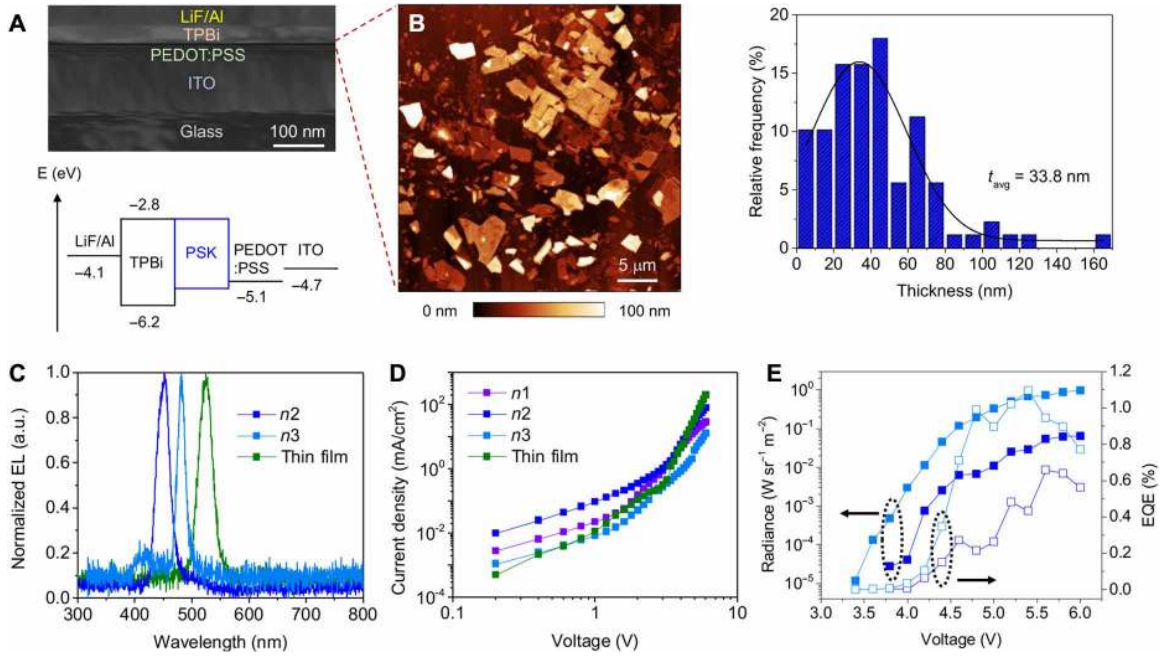

Fig. 3. Structure and device performance of the fabricated LED. (**A**) A cross-sectional SEM image and energy band alignment of the LED device. Conduction and valence bands are shown with respect to vacuum. (**B**) AFM image of the perovskite nanostructures with an average thickness of 34 nm. (**C**) EL spectra of *n*2 (blue), *n*3 (sky blue), and thin film (green)–based LED. (**D**) Voltage-dependent current density. (**E**) Voltage-dependent radiance (closed symbols) and EQE (open symbols) for *n*2 (blue) and *n*3 (sky blue) devices.

note that the EL spectrum peak of *n*1-based LED located at 410 nm (fig. S7A) is not conclusive because of an overlapped wavelength with TPBi emission (fig. S7B). Unlike the conventional spin-coated thin film–based approaches demonstrating energy funneling behaviors to the lowest bandgap and thus emitting their 3D bandgap wavelength (green line in Fig. 3C), this single-crystalline nanostructure-based LED device allows having an emission wavelength of the intrinsic bandgap of the corresponding RP crystal. The log-log curve of current density-voltage (*J*-*V*) is shown in Fig. 3D. Because of the randomly distributed RP crystals via a micromechanical exfoliation method, the *J*-*V* curves for each sample have no observable trends. The voltage-dependent radiance (closed squares) and EQE (open squares) for *n*2 (blue) and *n*3 (sky blue) are shown in Fig. 3E. The maximum EQEs for *n*2 and *n*3 devices are 0.7 and 1.1% at 5.6 and 5.4 V, respectively. This trend (i.e., higher EQE at lower emission energy) could reflect the lower electrical conductivity and the lower charge injection efficiencies of the wider bandgap semiconductors (fig. S5) (*8*). In comparison with previous efforts to crystallize thin films into polycrystalline via solvent vapor annealing for better emitting efficiency, our approach elevates the EQE significantly, which might be due to the high quality and single crystallinity of the RP phase single crystals. Also, our work demonstrates pure blue EL emission from the intrinsic bandgap without postsynthetic structural or additive engineering (*8*, *9*).

While we can successfully achieve pure blue light emission from the single-crystalline LED structure, the poor exfoliated sample uniformity and coverage (Fig. 3B) induces Joule heating and higher junction temperature under LED operation. From previous literature, it has already been proven that pinhole-free, thin, and smooth perovskite thin films can reduce the junction temperature and improve overall LED stability (*24*). During the operation, the junction temperature of our LED device has been estimated as shown in fig. S17 (for details, see the Supplementary Materials). When 6 V is continuously applied under LED operation, the junction temperature goes above 450 K in 10 s mainly due to the inhomogeneous perovskite layer, which can cause device degradation. A representative lifetime profile of the device is shown in fig. S18. For a deeper understanding of the high junction temperature–induced RP phase structure transformation/degradation, we have further pursued temperature-dependent PL study and the corresponding structure analysis.

Taking the *n*2 phase as we used for the blue-emitting LED demonstration, it is interesting that upon heating, the emission peak of the crystal became firstly asymmetrical with a long tail that developed at the longer wavelength side, and then a side peak was further developed at temperatures above 450 K, as shown in Fig. 4A. The side peak is the convolution of a series of emission peaks, which is more obvious in the *n*1 phase in situ heating PL spectra (fig. S8). Similar evolution features have also been observed in the *n*3 phase. These side-peak emissions in the *n*1 to *n*3 phases introduce a nearly pure white emission (for *n*1) and broad blue emissions (for *n*2 and *n*3) upon elevated temperatures (see CIE coordinate in fig. S9). After cooling to room temperature, the peak shape remains the same as the original one, indicating that the shape evolution during the heating/cooling process is reversible, although the peak intensity after the heating/cooling cycle is only about one-fifth of its original value (Fig. 4B). To understand the temperature-dependent spectra-structure dynamics, in situ temperature-dependent grazing-incidence wide-angle x-ray scattering (GIWAXS) and SCXRD crystal structure studies have been conducted (fig. S10 and tables S2 to S5). With the temperature increasing from 100 to 450 K, in situ SCXRD shows that the *a*-axis length expanded by 2.79% from 39.285 to 40.382 Å

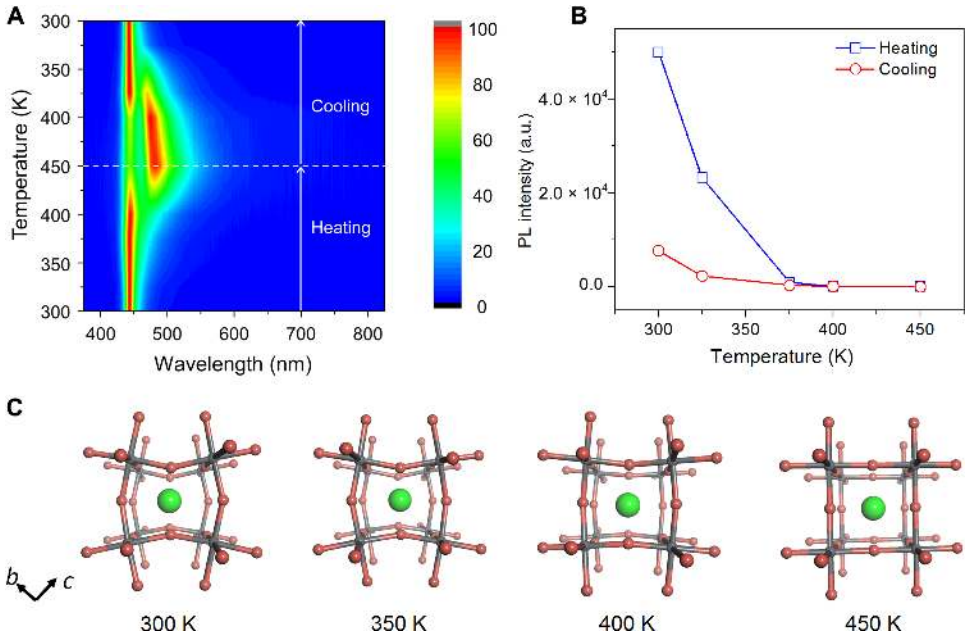

Fig. 4. Temperature-dependent PL and structure evolution of *n*2 phase single crystals. (**A**) Heating- and cooling-induced PL evolution of the *n*2 phase under nitrogen atmosphere above room temperature. (**B**) PL intensity variation during the heating and cooling process. (**C**) Temperature-dependent crystal structure evolution upon heating.

for the *n*2 phase, indicating that there is a thermal-introduced layer expansion during the heating process (fig. S12). Consistently, the crystallographic *b* and *c* axes also expanded by 0.84 and 2.51%, respectively. The anisotropic expansion of these two axes is attributed to the slight tilting of the in-plane $[PbBr_6]^{4-}$ octahedra (Fig. 4D). As the temperature increases from 100 to 400 K, the octahedra tend to be well aligned along the [100] axis. Upon heating the crystal to 450 K, a first-order phase transition happened, resulting in the orthorhombic to tetragonal space group transformation. Eventually, the crystal starts to melt, and the organic species between the perovskite layers partially decompose, which can be observed from the emerging PXRD ring feature and the thermal analysis (figs. S13 and S14). The PL and structure evolution dynamics indicate that careful control of the local temperature is critical for future improvement of the RP phase halide perovskite-based LED device stability.

Combining the observations from in situ PL and structure characterizations and DFT calculations, the evolution process of the temperature-dependent PL spectra can be ascribed to the tilting of the $[PbBr_6]^{4-}$ octahedra (Fig. 4C). As the structure obtained from SCXRD is an average structure model, a key parameter to reveal the thermal disorder tendency is the equivalent atomic displacement parameter, which quantifies the position uncertainty for each atom due to static and thermal disorder. Upon heating, the equivalent displacement parameters of all the atoms increased (fig. S15), which indicates broader range of atomic position distribution. This dynamical disorder thus introduces a diverse local structure configuration at the elevated temperatures (*25*). Since the different structure configuration can introduce different bandgaps as revealed by DFT modeling (fig. S16), the bandgap energy and PL emission tend to broaden, and the asymmetrical peak shape is developed toward higher wavelength range. The increase of structure disorder is understandable, as the high temperature can introduce large thermal disorder of the atoms. Moreover, as we heat the crystal in a non-equilibrium N_2 gas flow for SCXRD and in situ PL measurements, the exact equilibrium time for structure transformation from the initial model to the highly ordered stage is unknown. Multiple dynamic local configurations may coexist within the single crystals during this process; thus, the structure and spectra we measured at high temperatures are reflective of these multiple local configurations, leading to a broad PL spectrum including the original peak at around 445 nm of the *n*2 phase (*26*).

CONCLUSION

In this study, a series of Cs-Pb-Br–based blue-emissive pure RP phase single crystals were successfully synthesized by structural confinement engineering of perovskite layers with organic layers through a solution-based method. The PL emission intensity and peak position of these materials can be tuned across the blue light spectrum range by varying the inorganic octahedra layer thickness *n*. For pure blue EL demonstration, LED devices have been used based on micromechanical exfoliation of single crystals without postsynthetic structural or additive engineering. To elucidate the origin of the high junction temperature–induced LED device degradation, we further pursued the temperature-dependent in situ PL and structural analysis. With the illustration of in situ optical and structural evolutions, we concluded that the emission spectrum evolution of RP phase single crystals at high temperatures was mainly contributed by the increased atomic disordering as indicated by the evolution of the structural geometry and larger atomic displacement factors on the framework atoms. This work provides deep insights into the design and optimizes the RP phase halide perovskite single-crystalline materials–based blue-emissive LED. To drive the industrial application of 2D-halide perovskite materials for LEDs, better heat stability materials or heat management strategy for LED devices need to be developed in the future.

MATERIALS AND METHODS

RP phase single-crystal synthesis

Synthesis of the $(BA)_2Cs_{n-1}Pb_nBr_{3n+1}$ single crystal with different layer numbers (n)

Unless otherwise stated, all chemicals were purchased from Sigma-Aldrich and used as received. *n*-Butylammonium bromide ($C_4H_9NH_3Br$, BABr) was prepared and purified according to the method mentioned in our previous report (*27*). $(BA)_2Cs_{n-1}Pb_nBr_{3n+1}$ (n = 1 to 3) single crystals were synthesized as follows. Appropriate amounts of BABr, CsBr, and $PbBr_2$ powders were mixed together in saturated aqueous HBr solution in a sealed glass vial. The precursors were completely dissolved by heating to boiling under continuous stirring for about 30 min. Then, the solution was cooled down to room temperature, and colorless (n1) and yellow (n2 and n3) crystals started to precipitate in different recipe solutions. The crystals were collected by suction filtration and dried in vacuum before use. By fine-tuning the react chemical composition ratios, reaction temperature, and cooling rate, pure-phase single crystals can be obtained. For n1, the optimized mole ratio of BA/Cs/Pb in the precursors is about 2:0:1 at a reaction temperature of 120°C and a cooling rate of 1°C min^{-1}. For n2, the optimized mole ratio of BA/Cs/Pb is about 3:1:2 at a reaction temperature of 100°C and a cooling rate of 20°C min^{-1}. For n3, the optimized mole ratio of BA/Cs/Pb is about 3.5:2:3 at a reaction temperature of 100°C and a cooling rate of 20°C min^{-1}.

Crystal structure determination

Single-crystal x-ray diffraction

SCXRD data were all collected with a synchrotron radiation source (λ = 0.7749 Å) under N_2 atmosphere at beamline 11.3.1 at the Advanced Light Source, Lawrence Berkeley National Laboratory. Suitable single crystals of different compositions were mounted on a Bruker diffractometer using a Kapton tip. N_2 cryogen with a temperature controller was used to adjust the temperature used for in situ structure study. For each dataset, the crystal was equilibrated for 15 min after the dedicated temperature was reached, and the data collection time for each dataset is around 15 min. Data reduction was performed with APEX 3 software, and multiscan absorption correction was carried out with SADABS software. The crystal structure was solved with intrinsic phasing algorithm with SHELXT 2014 software and refined by full-matrix least-squares on F^2 with SHELXL (*28*). The detailed crystallographic information on the structure determination and refinement are listed in tables S1 to S4. All the crystallographic information files have been deposited in the Cambridge Crystallographic Data Centre with CCDC nos. 1945905 to 1945912.

Powder x-ray diffraction

Powder x-ray diffraction data were collected using a laboratory diffractometer with a Cu Kα (λ = 1.5418 Å) radiation source. GIWAXS data were collected at beamline 11-3 at the Stanford Synchrotron Radiation Lightsource (SSRL) with 12.4 keV energy. The grazing angle was set at 2°. The single crystals were ground carefully and dispersed on glass and loaded in a He chamber during the data collection period. A program-controlled temperature controller was used for data collection; for each temperature integer, the samples were equilibrated for 15 min after the dedicated temperature was reached and then collected for 1 min.

PL spectroscopy data collection

All the PL characterizations were measured with a PL microscope system. A continuous-wave solid-state laser (Coherent OBIS 375LX), which provides an excitation wavelength of 375 nm, was used as the light source. A more detailed description of the experimental setup can be found in our previous paper (*29*). Low-temperature PL was collected with a microscope cryostat (Janis Research Company ST-500) under vacuum (5×10^{-6} torr). PL spectra at high temperature were carried out in the same system coupled with an HCP422G gas-tight hot plate (Instec Inc., HCP422G) with a temperature controller. All the single-crystalline samples were held inside the chamber. Ar gas was continuously purged into the chamber, and the samples were heated from room temperature to 450 K with a heating controller. The quantum efficiency was determined with an integration sphere. The quantum efficiency was calculated from the ratio between the emission and the absorption spectra.

PL lifetime measurement

The carrier recombination lifetime of the samples was measured by a time-resolved PL system. A Ti:Sapphire laser system (Spectra-Physics Mai Tai) with a pulse width of less than 100 fs and a repetition rate of 80 MHz was used to excite the samples through 50× objective with 0.6 numerical aperture at an excitation wavelength of 400 nm (second-harmonic laser wavelength). The illuminating power was controlled by the neutral density filter. The PL signal was collected by the same objective and filtered by a long-pass filter (405 nm) before entering a controllable pinhole with a diameter of 50 μm in front of a Hamamatsu photomultiplier tube.

Other physical characterizations

Absorption spectra measurement

The absorption spectra were collected with a UV-3101 (Shimadzu) UV-vis spectrophotometer.

Thermogravimetry and differential scanning calorimeter

Thermogravimetry–differential scanning calorimeter curves were recorded by TA SDT Q600. Samples were dried under vacuum and then heated in a sealed Al pan from room temperature to 400°C under N_2 atmosphere with a heating rate of 5°C min^{-1}.

SEM and EDX spectroscopy

The morphologies of single crystals and EDX were analyzed by a field-emission SEM (JEOL JSM-6340F).

Electrical conductivity measurement

As-synthesized crystals were micromechanically exfoliated on a heavily p-doped 300-nm SiO_2/Si substrate. A transmission electron microscopy grid (200 mesh, SPI Supplies) was placed on the substrate, and electrodes (5 nm Cr and 95 nm Au) were deposited via electron beam deposition. During the device fabrication, the samples were exposed in ambient air for less than an hour. All measurements were done in high vacuum (~1×10^{-5} torr) at 80 K with liquid N_2 cooling.

AFM imaging

The topography measurements of micromechanically exfoliated n2 nanosheets were performed in tapping mode using a Park Systems AFM with Si cantilevers. Images (size, 50 μm by 50 μm) were obtained using a minimum of 512 samples per line with a scanning rate of 0.2 Hz.

LED device fabrication and characterization

Prepatterned ITO-coated substrates were subsequently ultrasonicated in deionized (DI) water with detergent, DI water, acetone, isopropyl alcohol, and DI water. The clean ITO substrates were then treated with O_2 plasma for 20 min for better wettability. PEDOT:PSS (Clevios

PVP AI 4083) solution was filtered with a 0.45-μm polyvinylidene difluoride syringe filter and spin-coated in air at 4000 rpm for 1 min followed by annealing at 150°C for 30 min in air. As-synthesized crystals were placed on adhesive tape with a size of 1 cm by 1 cm and peeled off repeatedly until the entire tape area looks uniform in color (yellow for *n*2 and *n*3 crystals and pale gray for *n*1 crystals). Then, the tape was directly placed on the prepared PEDOT:PSS layer and gently rubbed with Teflon tweezers under ambient conditions. The prepared layer was characterized via an AFM measurement as shown in Fig. 3B. The samples were then transferred in a thermal evaporator where layers of TPBi, lithium fluoride (LiF), and Al were sequentially deposited in an ultrahigh vacuum (2×10^{-6} mbar). LiF and Al were deposited with a metal shadow mask to define the cathodes. The *J*-*V* curve was measured using a Keithley 2636A source meter. The EL spectrum was collected using a microscopic PL spectroscopy setup at room temperature. Assuming a Lambertian emission profile, the EQE was extracted from optical power measurements using a Newport 818 UV photodiode connected to a Newport 1835-C multifunction optical meter.

The junction temperature in fig. S17 was estimated from the generalized Planck equation described from a previous study (*30*). Briefly, it was estimated from the slope of the high-energy tail of the emission spectrum based on the equation $\ln(I_{ref})/I) \sim E/k_B(1/T - 1/T_{ref})$, where I, E, k_B, and T are emission intensity, photon energy, Boltzmann's constant, and temperature, respectively.

DFT calculation

DFT calculations were carried out using the Vienna ab initio simulation package (*31*). The core-valence interaction was described by the projector-augmented wave method (*32*). The generalized gradient approximation of Perdew-Burke-Ernzerhof (*33*) was adopted for the exchange-correlation functional. The wave functions were expanded in a plane-wave basis set with a 300-eV cutoff. The experimentally measured crystal structures were used for calculations. Brillouin zone sampling was performed with a $2 \times 2 \times 2$ *k*-point mesh.

SUPPLEMENTARY MATERIALS

Supplementary material for this article is available at http://advances.sciencemag.org/cgi/content/full/6/4/eaay4045/DC1

Fig. S1. The PL spectrum of mixed phase products showing multiple peaks.
Fig. S2. SEM images and EDX spectra of different RP phase crystals.
Fig. S3. PXRD of the ground RP phase crystals.
Fig. S4. Low-temperature PL spectra of *n*1 to *n*3 single crystals.
Fig. S5. The photocurrent measurement of different RP phase crystals.
Fig. S6. PL stability of *n*3 single crystal.
Fig. S7. EL spectrum of *n*1 and TPBi-based LED devices.
Fig. S8. Normalized in situ temperature-dependent PL.
Fig. S9. CIE coordinate of *n*1 to *n*3 phases at the high temperature.
Fig. S10. In situ GIWAXS data of the RP phase crystals heated under a He chamber.
Fig. S11. The (400) crystallographic plane of the *n*2 phase, which directly goes through the BA^+ organic amine position.
Fig. S12. Temperature-dependent unit cell parameters of the *n*2 phase.
Fig. S13. Unwrap image of (0kl) of *n*2 based on in situ SCXRD.
Fig. S14. Thermal properties of the RP phases.
Fig. S15. Equivalent displacement parameters (Ueq) of framework atoms in the *n*2 phase.
Fig. S16. Band structures of the *n*2 phase under different temperatures.
Fig. S17. Extracted device junction temperature under LED operation at 6 V.
Fig. S18. A lifetime of the *n*2-based LED device with an initial power of 10 μW cm^{-2}.
Fig. S19. EL spectra evolution operated at 10 V.
Table S1. Crystallographic refinement data of different RP phases at 100 K.
Table S2. Crystal data and structure refinement details for *n*2.
Table S3. Unit cell parameters and space group evolution of *n*2 from 100 to 450 K under in situ heating environment.
Table S4. Unit cell parameters and space group evolution of *n*2 from 450 to 100 K under in situ cooling environment.
Table S5. Bond angle and atomic distances of an *n*2 structure building unit under different temperatures.

REFERENCES AND NOTES

1. S. D. Stranks, H. J. Snaith, Metal-halide perovskites for photovoltaic and light-emitting devices. *Nat. Nanotechnol.* **10**, 391–402 (2015).
2. S. A. Veldhuis, P. P. Boix, N. Yantara, M. Li, T. C. Sum, N. Mathews, S. G. Mhaisalkar, Perovskite materials for light-emitting diodes and lasers. *Adv. Mater.* **28**, 6804–6834 (2016).
3. B. R. Sutherland, E. H. Sargent, Perovskite photonic sources. *Nat. Photonics* **10**, 295–302 (2016).
4. K. Lin, J. Xing, L. N. Quan, F. P. G. de Arquer, X. Gong, J. Lu, L. Xie, W. Zhao, D. Zhang, C. Yan, W. Li, X. Liu, Y. Lu, J. Kirman, E. H. Sargent, Q. Xiong, Z. Wei, Perovskite light-emitting diodes with external quantum efficiency exceeding 20 per cent. *Nature* **562**, 245–248 (2018).
5. Y. Cao, N. Wang, H. Tian, J. Guo, Y. Wei, H. Chen, Y. Miao, W. Zou, K. Pan, Y. He, H. Cao, Y. Ke, M. Xu, Y. Wang, M. Yang, K. Du, Z. Fu, D. Kong, D. Dai, Y. Jin, G. Li, H. Li, Q. Peng, J. Wang, W. Huang, Perovskite light-emitting diodes based on spontaneously formed submicrometre-scale structures. *Nature* **562**, 249–253 (2018).
6. M. K. Gangishetty, S. Hou, Q. Quan, D. N. Congreve, Reducing architecture limitations for efficient blue perovskite light-emitting diodes. *Adv. Mater.* **30**, e1706226 (2018).
7. J. Byun, H. Cho, C. Wolf, M. Jang, A. Sadhanala, R. H. Friend, H. Yang, T.-W. Lee, Efficient visible quasi-2D perovskite light-emitting diodes. *Adv. Mater.* **28**, 7515–7520 (2016).
8. S. Kumar, J. Jagielski, S. Yakunin, P. Rice, Y.-C. Chiu, M. Wang, G. Nedelcu, Y. Kim, S. Lin, E. J. G. Santos, M. V. Kovalenko, C.-J. Shih, Efficient blue electroluminescence using quantum-confined two-dimensional perovskites. *ACS Nano* **10**, 9720–9729 (2016).
9. D. Liang, Y. Peng, Y. Fu, M. J. Shearer, J. Zhang, J. Zhai, Y. Zhang, R. J. Hamers, T. L. Andrew, S. Jin, Color-pure violet-light-emitting diodes based on layered lead halide perovskite nanoplates. *ACS Nano* **10**, 6897–6904 (2016).
10. B. Saparov, D. B. Mitzi, Organic–inorganic perovskites: Structural versatility for functional materials design. *Chem. Rev.* **116**, 4558–4596 (2016).
11. C. C. Stoumpos, C. M. M. Soe, H. Tsai, W. Nie, J.-C. Blancon, D. H. Cao, F. Liu, B. Traoré, C. Katan, J. Even, A. D. Mohite, M. G. Kanatzidis, High members of the 2D Ruddlesden-Popper halide perovskites: Synthesis, optical properties, and solar cells of $(CH_3(CH_2)_3NH_3)_2(CH_3NH_3)_4Pb_5I_{16}$. *Chem* **2**, 427–440 (2017).
12. Z. Wang, Q. Lin, F. P. Chmiel, N. Sakai, L. M. Herz, H. J. Snaith, Efficient ambient-air-stable solar cells with 2D–3D heterostructured butylammonium-caesium-formamidinium lead halide perovskites. *Nat. Energy* **2**, 17135 (2017).
13. C. C. Stoumpos, D. H. Cao, D. J. Clark, J. Young, J. M. Rondinelli, J. I. Jang, J. T. Hupp, M. G. Kanatzidis, Ruddlesden–Popper hybrid lead iodide perovskite 2D homologous semiconductors. *Chem. Mater.* **28**, 2852–2867 (2016).
14. X. Yang, X. Zhang, J. Deng, Z. Chu, Q. Jiang, J. Meng, P. Wang, L. Zhang, Z. Yin, J. You, Efficient green light-emitting diodes based on quasi-two-dimensional composition and phase engineered perovskite with surface passivation. *Nat. Commun.* **9**, 570 (2018).
15. M. Yuan, L. N. Quan, R. Comin, G. Walters, R. Sabatini, O. Voznyy, S. Hoogland, Y. Zhao, E. M. Beauregard, P. Kanjanaboos, Z. Lu, D. H. Kim, E. H. Sargent, Perovskite energy funnels for efficient light-emitting diodes. *Nat. Nanotechnol.* **11**, 872–877 (2016).
16. N. Wang, L. Cheng, R. Ge, S. Zhang, Y. Miao, W. Zou, C. Yi, Y. Sun, Y. Cao, R. Yang, Y. Wei, Q. Guo, Y. Ke, M. Yu, Y. Jin, Y. Liu, Q. Ding, D. Di, L. Yang, G. Xing, H. Tian, C. Jin, F. Gao, R. H. Friend, J. Wang, W. Huang, Perovskite light-emitting diodes based on solution-processed self-organized multiple quantum wells. *Nat. Photonics* **10**, 699–704 (2016).
17. R. Quintero-Bermudez, A. Gold-Parker, A. H. Proppe, R. Munir, Z. Yang, S. O. Kelley, A. Amassian, M. F. Toney, E. H. Sargent, Compositional and orientational control in metal halide perovskites of reduced dimensionality. *Nat. Mater.* **17**, 900–907 (2018).
18. P. Vashishtha, M. Ng, S. B. Shivarudraiah, J. E. Halpert, High efficiency blue and green light-emitting diodes using Ruddlesden–Popper inorganic mixed halide perovskites with butylammonium interlayers. *Chem. Mater.* **31**, 83–89 (2019).
19. J. Xing, Y. Zhao, M. Askerka, L. N. Quan, X. Gong, W. Zhao, J. Zhao, H. Tan, G. Long, L. Gao, Z. Yang, O. Voznyy, J. Tang, Z.-H. Lu, Q. Xiong, E. H. Sargent, Color-stable highly luminescent sky-blue perovskite light-emitting diodes. *Nat. Commun.* **9**, 3541 (2018).
20. C. M. M. Soe, W. Nie, C. C. Stoumpos, H. Tsai, J.-C. Blancon, F. Liu, J. Even, T. J. Marks, A. D. Mohite, M. G. Kanatzidis, Understanding film formation morphology and orientation in high member 2D Ruddlesden–Popper perovskites for high-efficiency solar cells. *Adv. Energy Mater.* **8**, 1700979 (2018).
21. C. M. M. Soe, G. P. Nagabhushana, R. Shivaramaiah, H. Tsai, W. Nie, J.-C. Blancon, F. Melkonyan, D. H. Cao, B. Traoré, L. Pedesseau, M. Kepenekian, C. Katan, J. Even,

T. J. Marks, A. Navrotsky, A. D. Mohite, C. C. Stoumpos, M. G. Kanatzidis, Structural and thermodynamic limits of layer thickness in 2D halide perovskites. *Proc. Natl. Acad. Sci. U.S.A.* **116**, 58–66 (2019).
22. X. Wu, M. T. Trinh, D. Niesner, H. Zhu, Z. Norman, J. S. Owen, O. Yaffe, B. J. Kudisch, X.-Y. Zhu, Trap states in lead iodide perovskites. *J. Am. Chem. Soc.* **137**, 2089–2096 (2015).
23. M. Kulbak, S. Gupta, N. Kedem, I. Levine, T. Bendikov, G. Hodes, D. Cahen, Cesium enhances long-term stability of lead bromide perovskite-based solar cells. *J. Phys. Chem. Lett.* **7**, 167–172 (2016).
24. L. Zhao, K. M. Lee, K. Roh, S. U. Z. Khan, B. P. Rand, Improved outcoupling efficiency and stability of perovskite light-emitting diodes using thin emitting layers. *Adv. Mater.* **31**, 1805836 (2019).
25. A. Gold-Parker, P. M. Gehring, J. M. Skelton, I. C. Smith, D. Parshall, J. M. Frost, H. I. Karunadasa, A. Walsh, M. F. Toney, Acoustic phonon lifetimes limit thermal transport in methylammonium lead iodide. *Proc. Natl. Acad. Sci. U.S.A.* **115**, 11905–11910 (2018).
26. C. Quarti, E. Mosconi, J. M. Ball, V. D'Innocenzo, C. Tao, S. Pathak, H. J. Snaith, A. Petrozza, F. De Angelis, Structural and optical properties of methylammonium lead iodide across the tetragonal to cubic phase transition: Implications for perovskite solar cells. *Energ. Environ. Sci.* **9**, 155–163 (2016).
27. L. Dou, A. B. Wong, Y. Yu, M. Lai, N. Kornienko, S. W. Eaton, A. Fu, C. G. Bischak, J. Ma, T. Ding, N. S. Ginsberg, L.-W. Wang, A. P. Alivisatos, P. Yang, Atomically thin two-dimensional organic-inorganic hybrid perovskites. *Science* **349**, 1518–1521 (2015).
28. G. M. Sheldrick, Crystal structure refinement with SHELXL. *Acta Crystallogr. C* **71**, 3–8 (2015).
29. J. Lin, H. Chen, J. Kang, L. N. Quan, Z. Lin, Q. Kong, M. Lai, S. Yu, L. Wang, L.-w. Wang, M. F. Toney, P. Yang, Copper (I)-based highly emissive all-inorganic rare-earth halide clusters. *Matter* **1**, 180–191 (2019).
30. Y. Jia, R. A. Kerner, A. J. Grede, A. N. Brigeman, B. P. Rand, N. C. Giebink, Diode-pumped organo-lead halide perovskite lasing in a metal-clad distributed feedback resonator. *Nano Lett.* **16**, 4624–4629 (2016).
31. G. Kresse, J. Furthmüller, Efficient iterative schemes for ab initio total-energy calculations using a plane-wave basis set. *Phys. Rev. B* **54**, 11169–11186 (1996).
32. G. Kresse, D. Joubert, From ultrasoft pseudopotentials to the projector augmented-wave method. *Phys. Rev. B* **59**, 1758–1775 (1999).
33. J. P. Perdew, K. Burke, M. Ernzerhof, Generalized gradient approximation made simple. *Phys. Rev. Lett.* **77**, 3865–3868 (1996).

Acknowledgments
Funding: This work was supported by the U.S. Department of Energy, Office of Science, Office of Basic Energy Sciences, Materials Sciences and Engineering Division, under contract no. DE-AC02-05CH11231 within the Physical Chemistry of Inorganic Nanostructures Program (KC3103). The research used resources at the Stanford Synchrotron Radiation Light Source at SLAC National Accelerator Laboratory supported by the U.S. Department of Energy, Office of Science, Basic Energy Sciences under contract no. DE-AC02-76SF00515. The research also used resources at the Advanced Light Source, which is a DOE Office of Science User Facility under contract no. DE-AC02-05CH11231. H.C. acknowledges the postdoctoral scholarship support from the Wallenberg Foundation through the MAX IV synchrotron radiation facility program and the National Natural Science Foundation of China (21777045). J.L. acknowledges the fellowship support from the Shanghai University of Electric Power and the National Natural Science Foundation of China (61875119). J.K. acknowledges IBS Global Postdoctoral Fellowship (IBS-R026-D1). M.F.T. acknowledges support from the Center for Hybrid Organic Inorganic Semiconductors for Energy (CHOISE), an Energy Frontier Research Center funded by the Office of Basic Energy Sciences, Office of Science within the U.S. Department of Energy through contract no. DE-AC36-08G028308. **Author contributions:** H.C., J.L., and Joohoon Kang contributed equally to this work. H.C., J.L., Joohoon Kang, P.Y., and M.F.T. conceived the idea and designed the study. H.C. and J.L. pursued the overall experimental work. Joohoon Kang and Q.K. conceived the LED device fabrication. D.L., M.L., L.N.Q., Z.L., and J.J. helped with the optical characterizations. Jun Kang and L.W. performed the DFT modeling. Q.K. performed the EDX measurement. H.C., J.L., Joohoon Kang, P.Y., and M.F.T. wrote the manuscript. All authors discussed the results and revised the manuscript. **Competing interests:** The authors declare that they have no competing interests. **Data and materials availability:** All data needed to evaluate the conclusions in the paper are present in the paper and/or the Supplementary Materials. Additional data related to this paper may be requested from the authors.

Submitted 15 June 2019
Accepted 20 November 2019
Published 24 January 2020
10.1126/sciadv.aay4045

Citation: H. Chen, J. Lin, J. Kang, Q. Kong, D. Lu, J. Kang, M. Lai, L. N. Quan, Z. Lin, J. Jin, L.-w. Wang, M. F. Toney, P. Yang, Structural and spectral dynamics of single-crystalline Ruddlesden-Popper phase halide perovskite blue light-emitting diodes. *Sci. Adv.* **6**, eaay4045 (2020).

ScienceAdvances

Structural and spectral dynamics of single-crystalline Ruddlesden-Popper phase halide perovskite blue light-emitting diodes

Hong Chen, Jia Lin, Joohoon Kang, Qiao Kong, Dylan Lu, Jun Kang, Minliang Lai, Li Na Quan, Zhenni Lin, Jianbo Jin, Lin-wang Wang, Michael F. Toney and Peidong Yang

Sci Adv **6** (4), eaay4045.
DOI: 10.1126/sciadv.aay4045